Solution−Liquid−Solid Growth of Ternary Cu−In−Se Semiconductor Nanowires from Multiple- and Single-Source Precursors

Alfred J. Wooten, Donald J. Werder, Darrick J. Williams, Joanna L. Casson, and Jennifer A. Hollingsworth*

Chemistry Division and Center for Integrated Nanotechnologies, Los Alamos National Laboratory, Los Alamos, New Mexico 87545

Received July 10, 2009; E-mail: jenn@lanl.gov

Abstract: Ternary CuInSe$_2$ nanowires were synthesized for the first time by the solution−liquid−solid (SLS) mechanism. Here, both metal−organic multiple- and single-source molecular precursors were thermally decomposed in the presence of molten metal nanoparticles and coordinating ligands. The nature of the precursor—multiple- compared to single-source (wherein Cu−Se−In bonds are effectively preformed)—as well as the choice of coordinating ligands, reaction temperature, and reactant order-of-addition strongly affected the morphology and composition of the reaction product obtained. Crystalline, straight, and nearly stoichiometric CuInSe$_2$ nanowires were most readily achieved using the single-source precursor; however, careful tuning of reaction conditions could also be used to obtain high-quality nanowires from multiple-source precursor systems. The CuInSe$_2$ nanowires are strong light absorbers from the near-infrared through the visible and ultraviolet spectral regions and, thereby, comprise new soluble and processable "building blocks" for applications in solar-light harvesting.

Introduction

Nanoscale semiconductors are characterized by several unique and important properties that suggest potential utility for a range of applications and contrast them with their respective bulk-phase counterparts: (1) size-tunable band gap energies,[1,2] (2) lower thermally induced leakage currents (quantum confinement effects lead to an electronic density of states that is pushed away from the Fermi level), and (3) the potential for enhanced device efficiencies through carrier multiplication.[3,4] While much of the early work on the unique properties of confined dimensionality has involved three-dimensionally confined nanoparticles, or quantum dots (QDs), two-dimensionally confined nanowires (NWs) are expected to exhibit similar enabling characteristics. Further, NWs, by virtue of their "wire-like" geometry, offer the additional advantage of providing a built-in conduit for exciton diffusion and charge transport. Thus, semiconductor NWs comprise an important class of nanomaterials that have significant promise as active components in nanoenabled electronic and optoelectronic devices for applications from sensors to field-effect transistors, logic gates, light emission, energy harvesting, and energy storage.[5−8]

A materials class with particular relevance for *solar* energy harvesting is the I−III−VI$_2$ group of compounds, where the group I metal is typically Cu, the group III metal is typically In or Ga, and the group VI element is generally Se or S. By controlling composition, the direct band gap energy for this group can be tuned from ~2.5 to ~1.03 eV (the bulk band gap energies of the compositional end points, CuGaS$_2$ and CuInSe$_2$, respectively) to optimize collection of the available solar flux. Further band gap tuning can be achieved through quantum confinement effects by restricting and controlling particle size below the size of the Bohr exciton radius (10.6 nm for CuInSe$_2$).[9] In addition to possessing a "solar-active" band gap energy range, this group of compound semiconductors exhibits exceptional radiation hardness and defect tolerance[10] and has provided record efficiencies in the form of thin-film photovoltaic devices, for example, 19.9%[11] for CuIn$_x$Ga$_{1−x}$Se$_2$ (CIGS) and 25.8%[12] for multijunction GaAs/CuInSe$_2$ thin-film modules. While the thin-film structures reflect the outstanding bulk-phase properties of the I−III−VI$_2$ group of compounds, nanoscale versions of these materials are desirable as alternative "building

(1) Pietryga, J. M.; Schaller, R. D.; Werder, D.; Stewart, M. H.; Klimov, V. I.; Hollingsworth, J. A. *J. Am. Chem. Soc.* **2004**, *126*, 11752–11753.
(2) Hollingsworth, J. A. Semiconductor Nanocrystal Quantum Dots. *Encyclopedia of Inorganic Chemistry*, 2nd ed.; John Wiley & Sons, Ltd.: New York, 2005; Vol. VIII.
(3) Schaller, R. D.; Sykora, M.; Pietryga, J. M.; Klimov, V. I. *Nano Lett.* **2006**, *6*, 424–429.
(4) Schaller, R. D.; Klimov, V. I. *Phys. Rev. Lett.* **2004**, *92*, 186601.

(5) Tian, B.; Zheng, X.; Kempa, T. J.; Fang, Y.; Yu, N.; Yu, G.; Huang, J.; Lieber, C. M. *Nature* **2007**, *449*, 885–889.
(6) Persson, A. I.; Bjork, M. T.; Jeppesen, S.; Wagner, J. B.; Wallenberg, L. R.; Samuelson, L. *Nano Lett.* **2006**, *6*, 403–407.
(7) Wang, F.; Dong, A.; Sun, J.; Tang, R.; Yu, H.; Buhro, W. E. *Inorg. Chem.* **2006**, *45*, 7511–7521.
(8) Chan, C. K.; Peng, H.; Liu, G.; McIlwrath, K.; Zhang, X. F.; Huggins, R. A.; Cui, Y. *Nat. Nano* **2008**, *3*, 31–35.
(9) Castro, S. L.; Bailey, S. G.; Raffaelle, R. P.; Banger, K. K.; Hepp, A. F. *Chem. Mater.* **2003**, *15*, 3142–3147.
(10) Zhang, S. B.; Wei, S.-H.; Zunger, A.; Katayama-Yoshida, H. *Phys. Rev. B* **1998**, *57*, 9642.
(11) Repins, I.; Contreras, M. A.; Egaas, B.; DeHart, C.; Scharf, J.; Perkins, C. L.; To, B.; Noufi, R. *Prog. Photovoltaics* **2008**, *16*, 235–239.
(12) Martin, A. G.; Keith, E.; David, L. K.; Yoshihiro, H.; Wilhelm, W. *Prog. Photovoltaics* **2007**, *15*, 35–40.

blocks" for solar energy harvesting, affording the potential for multiexciton-generation-enhanced efficiencies[3] and facile, low-cost, low-energy fabrication and processing. Nanoscale I−III−VI$_2$ materials can also function as ideal "test subjects" for studying and understanding fundamental properties influencing device efficiencies.[13] While several reports describe the preparation of high-quality *isotropic* I−III−VI$_2$ nanomaterials,[14−18] as well as CuIn$_5$Se$_8$ and CuIn$_{2.3}$Se$_4$ colloidal nanocrystals,[19] fewer such reports are yet available for *anisotropic* I−III−VI$_2$ NWs, and the most successful of these are vapor-phase preparations.[13,20] Thus, there remains a need for new methods for the synthesis of high-quality CIGS NWs, especially solution-phase preparations. To this end, we describe here the first solution-phase synthesis of highly crystalline, regularly shaped CuInSe$_2$ NWs.

In general, semiconductor NWs can be fabricated using either vapor- or solution-phase methods, where solution-phase approaches commonly afford the advantages of lower growth temperatures and facile, lower-cost processing. To date, solution growth of high-quality NWs has been reported for numerous materials systems (e.g., InP, InAs, GaP, GaAs, ZnTe, CdSe, CdTe, PbSe, ZnO),[7,21] but as described above, similar reports for I−III−VI$_2$ NW systems are lacking. The limited examples of solution-phase preparations for anisotropic I−III−VI$_2$ nanocrystals have involved either molecular or anodized alumina templating strategies. Specifically, Yang et al.[22] employed a molecular template to synthesize CuInSe$_2$ nanorods (50−100 nm in diameter and several micrometer in length) in a lengthy (32−48 h) solvothermal reaction. Further, Phok et al.[23] employed a porous alumina template to synthesize irregularly shaped CuInSe$_2$ NWs (5−40 nm in diameter and several micrometer in length) by electrodeposition into the template followed by a postreaction annealing step. In contrast, the most successful CuInSe$_2$ NW preparation to date[13] utilized a *nontemplated* vapor-phase approach known as vapor−liquid−solid (VLS) growth to synthesize low-defect single-crystalline NWs (20−200 nm in diameter and up to >100 μm in length). The VLS approach employs Au nanoparticles that facilitate the anisotropic growth of semiconductor NWs and, simultaneously, control the diameter of the NW.

A solution-phase analogue to VLS exists and is known as solution−liquid−solid (SLS) growth. SLS also employs metal nanoparticles as NW-growth "catalysts" (Figure 1) and is capable of producing high-quality, single-crystalline NWs.[7,21] Compared to other approaches, the SLS method provides access
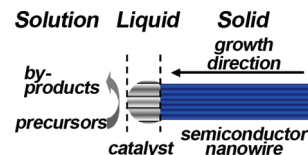

Figure 1. Schematic of the solution−liquid−solid NW growth mechanism.

to NWs that possess a unique set of characteristics. Namely, the approach and resulting nanomaterials are characterized by facile, low-temperature solution-phase preparation (amenable to scale-up), the ability to control NW diameter (as a function of metal catalyst size), even to the quantum-confined regime (typically <10 nm), high crystallinity, and surface "passivation" afforded by surface-bound organic molecules ("ligands").[7,21] The presence of a ligand layer on the SLS-grown NWs renders them soluble in a range of nonpolar solvents and can improve or modify functional properties such as photoluminescence and electrical transport. To date, SLS has been used successfully to demonstrate the synthesis of a wide range of binary (II−VI, III−V, IV−VI)[7,21] and even heterostructured II−VI[24,25] NW systems. However, to the best of our knowledge, the use of the SLS method in *the direct and targeted synthesis of higher order ternary semiconductor NWs that contain metal cations with different oxidation states has yet to be demonstrated*. In contrast, the only existing demonstration of the SLS synthesis of ternary NWs resulted from an attempt to prepare ZnSe−ZnTe NW heterostructures. In this case, the alloyed ternary compound, ZnSe$_x$Te$_{1−x}$, was also obtained, where the anionic composition varied along the length of the wire.[24]

As a result of the technological significance of CuInSe$_2$ (and related I−III−VI$_2$ materials), as well as the unique opportunity afforded by the SLS growth mechanism to realize high-quality NWs, we sought to demonstrate for the first time the nontemplated solution-phase synthesis of CuInSe$_2$ NWs by this method. As alluded to above, the ternary nature of this relatively complex system, where the metals are characterized by disparate oxidation states, was considered a synthetic challenge. Further, in contrast with comparable II−VI binary systems (ZnSe, CdS), I−III−VI$_2$ materials tolerate a large degree of "off-stoichiometry" in terms of Cu/In/Se ratios.[10] For this reason, the resulting composition of a given NW was expected to be particularly sensitive to the relative reactivities of the metal and chalcogenide precursors (perhaps more so than for a simple binary system with limited tolerance for compositions that deviate from stoichiometric). Therefore, we explored not only the use of multiple-source precursors for the synthesis of CuInSe$_2$ but also the use of a single-source precursor, as well. The latter provides the Cu, In, and Se components with "preformed" metal−chalcogenide−metal bonds, ideally facilitating more uniform incorporation into the final NW product.

Experimental Section

General Methods. All reactions and manipulations were carried out with oven-dried glassware under inert atmosphere conditions using standard Schlenk line techniques or a drybox, up until reaction quenching. Oleic acid [Aldrich, 90%], In(O$_2$CCH$_3$)$_3$ [Strem, 99.9995%], Cu(O$_2$CCH$_3$) [Strem, 97%], [Cu(MeCN)$_4$]$^+$PF$_6^-$ [Strem, 98+%], Ph$_3$P [Acros, 99%], anhydrous InCl$_3$ [Strem, 99.999%],

(13) Peng, H.; Schoen, D. T.; Meister, S.; Zhang, X. F.; Cui, Y. *J. Am. Chem. Soc.* **2007**, *129*, 34−35.

(14) Castro, S. L.; Bailey, S. G.; Raffaelle, R. P.; Banger, K. K.; Hepp, A. F. *J. Phys. Chem. B* **2004**, *108*, 12429−12435.

(15) Guo, Q.; Kim, S. J.; Kar, M.; Shafarman, W. N.; Birkmire, R. W.; Stach, E. A.; Agrawal, R.; Hillhouse, H. W. *Nano Lett.* **2008**, *8*, 2982−2987.

(16) Zhong, H.; Li, Y.; Ye, M.; Zhu, Z.; Zhou, Y.; Yang, C.; Li, Y. *Nanotechnology* **2007**, *18*, 025602.

(17) Nakamura, H.; Kato, W.; Uehara, M.; Nose, K.; Omata, T.; Otsuka-Yao-Matsuo, S.; Miyazaki, M.; Maeda, H. *Chem. Mater.* **2006**, *18*, 3330−3335.

(18) Panthani, M. G.; Akhavan, V.; Goodfellow, B.; Schmidtke, J. P.; Dunn, L.; Dodabalapur, A.; Barbara, P. F.; Korgel, B. A. *J. Am. Chem. Soc.* **2008**, *130*, 16770−16777.

(19) Allen, P. M.; Bawendi, M. G. *J. Am. Chem. Soc.* **2008**, *130*, 9240−9241.

(20) Peng, H.; Xie, C.; Schoen, D. T.; McIlwrath, K.; Zhang, X. F.; Cui, Y. *Nano Lett.* **2007**, *7*, 3734−3738.

(21) Kuno, M. *Phys. Chem. Chem. Phys.* **2008**, *10*, 620−639.

(22) Yang, Y. H.; Chen, Y. T. *J. Phys. Chem. B* **2006**, *110*, 17370−17374.

(23) Phok, S.; Rajaputra, S.; Singh, V. P. *Nanotechnology* **2007**, *18*, 475601.

(24) Dong, A.; Wang, F.; Daulton, T. L.; Buhro, W. E. *Nano Lett.* **2007**, *7*, 1308−1313.

(25) Ouyang, L.; Maher, K. N.; Yu, C. L.; McCarty, J.; Park, H. *J. Am. Chem. Soc.* **2007**, *129*, 133−138.

NaOEt [Fluka, ≥95(T)%], C_6H_5SeH [Strem, 97%], $BiCl_3$ [Acros, 99.999%], and *n*-BuMgCl [Aldrich, 2.0 M solution in diethyl ether] were all used without additional purification. HPLC grade acetone, toluene, hexanes, and chloroform were all purchased from Aldrich and used without additional purification. Anhydrous solvents, methanol [Aldrich, 99.8%], 1,2-dichlorobezene [Aldrich, 99%], diphenyl ether [Acros, 99%], diethyl ether [Aldrich, ≥99.7%], trioctylphosphine oxide (TOPO) [Acros, 99%], trioctylamine (TOA) [Aldrich, 98%] and *n*-octadecylphosphonic acid [Alfa Aesar, crystalline solid] were also used without further purification. Trioctylphosphine (TOP) [Strem, 90%] was prepurified by heating the solvent to 200 °C under vacuum for 2 h. Then, 1.0 M solutions of trioctylphosphine selenium (TOPSe) were prepared in advance of use by stirring overnight appropriate amounts of purified TOP and selenium pellets [Aldrich, ~2 mm, 99.999%] inside the drybox at room temperature. Postpreparative handling and spectroscopy were conducted under ambient conditions.

Synthesis of Gold Nanoparticles ($Au_{101}(PPh_3)_{21}Cl_5$, Au-NPs). The Au-NPs were synthesized according to the procedure reported by Hutchison et al.,[26] which was modified slightly. Briefly, the procedure was carried out as follows: $HAuCl_4$ (0.5 g, 1.25 mmol) and tetraoctylammonium bromide (0.80 g, 1.47 mmol) were dissolved in a water/toluene (50 mL:65 mL) mixture inside a Schlenk flask under nitrogen flow. This mixture was then degassed under vacuum for ~5 min at room temperature. Under nitrogen flow, the solution was stirred vigorously at room temperature until the golden color had transferred into the organic phase. Triphenylphosphine (1.16 g, 4.43 mmol) was then added, and the solution was stirred vigorously for an additional 15–30 min, until the organic phase turned white and cloudy. The cloudy solution was then cooled to 0 °C using an ice bath. An aqueous solution of sodium borohydride was prepared immediately prior to use, by dissolving (0.705 g, 18.65 mmol) this reagent in 10 mL of deionized water, and rapidly added to the cooled cloudy solution (this addition results in vigorous bubbling and should be performed cautiously). The reaction mixture was stirred at 0 °C for an additional 5 min before the ice bath was removed. Gradually warming to room temperature, the organic phase progressively turned dark purple after which time it was stirred for an additional 3 h under nitrogen flow. The toluene layer was then separated and washed twice with 100 mL of deionized water. All volatiles were removed in vacuo to yield a dark-purplish solid.

Additional Purification Procedure for the Au-NPs. The resulting dark-purplish solid was washed with a series of solvents (hexanes, saturated aqueous sodium nitrite, and a 2:3 methanol/water mixture) to remove the phase transfer catalyst, byproducts, and unreacted starting materials. This additional washing procedure was followed exactly according to the published procedure by Hutchison et al.[26] After the additional washing steps, the dark-purplish solid was dissolved in chloroform and the solution was filtered through a medium frit to remove any insoluble materials. The deep purple solution was reduced in volume to ~50 mL under vacuum. After warming the solution to room temperature, pentane (120 mL, HPLC grade) was added slowly to precipitate the product, yielding 0.5 g of purified Au-NPs. The Au-NPs (0.5 g, 0.0195 mmol) were dissolved in 65 mL of toluene to generate a 0.0003 M (0.3 mM) stock solution.

Synthesis of Tributylbismuth (Bi(*n*-Bu)₃). The Bi(*n*-Bu)₃ precursor was synthesized according to a modified version of the procedure previously reported by Mitzi.[27] A three-neck flask was charged with $BiCl_3$ (1.89 g, 6.0 mmol) and dissolved in 100 mL of anhydrous diethyl ether, followed by slow addition of *n*-BuMgCl (9 mL, 18.0 mmol, 2.0 M solution in diethyl ether) to the reaction flask inside the drybox. Upon addition of *n*-BuMgCl, a white precipitate immediately formed and the solvent began to bubble

slightly as a result of the exothermic reaction. After complete addition of the Grignard reagent, the reaction slowly cooled to room temperature and was allowed to stir inside the drybox for 18 h. The cloudy mixture was then filtered through a fine glass frit, and a clear and cloudless solution was obtained. All volatile materials were removed in vacuo, yielding a viscous liquid that contained a white precipitate. Anhydrous pentane was then added to this viscous liquid and filtered once more through a fine glass frit, whereby a clear colorless solution containing the product was isolated. All volatile materials were removed in vacuo, yielding 2.06 g of a clear viscous liquid (90% yield based on $BiCl_3$). A 1.0 M stock solution was then prepared by dissolving 2.06 g of the product in 6.0 mL of solvent (4.8 mL of toluene and 1.2 mL of diphenyl ether) and stored inside the drybox freezer and used directly.

Synthesis of (Gold)Bismuth (Core)Shell Catalyst Nanoparticles. The (Au)Bi catalyst particles were synthesized according to procedures reported by Kuno et al.[28,29] Typically, the procedure was carried out as follows: a mixture of phenyl ether (4.00 mL, 25.2 mmol), TOP (0.600 mL, 1.34 mmol), and 2.5 mL (0.75 µmol) of the 0.3 mM Au-NP stock solution prepared above was added to a three-neck flask. This mixture was then heated to 100 °C under vacuum to dry and degas the reagents, after which time (~20 min) the reaction flask was backfilled with N_2. In a glovebox, an injection solution containing phenyl ether (4.00 mL, 25.2 mmol), TOP (0.600 mL, 1.34 mmol), and Bi(*n*-Bu)₃ (0.615 mmol, 0.615 mL of a 1.0 M stock solution) was prepared. Toluene (3.0 mL) was combined with the 5.215 mL injection solution to aid solubility of Bi(*n*-Bu)₃, and this mixture was then delivered to the Au-NP solution with a syringe pump at a nominal rate of 7 mL/h. Upon addition of the Bi(*n*-Bu)₃ mixture, the reaction solution turned progressively darker, with no observed plating of bismuth. After ~1.7 h of slow syringe pump addition, the reaction mixture was allowed to cool to room temperature, and the resulting (Au)Bi NPs were precipitated by gradual addition of 17.5 mL of acetonitrile. Care was taken to prevent adding an excess of acetonitrile as this leads to a phase separation, which complicates recovery of the (Au)Bi-NPs. The suspension was then centrifuged at 4300 rpm for 10 min to obtain the (Au)Bi-NP precipitate, which was redissolved in 2.0 mL of toluene along with a few drops of oleic acid (0.03 mL). The concentration of the (Au)Bi NP catalyst solution was normalized to an absorbance value of $A = 0.1235$ at 500 nm, yielding an estimated NP stock concentration of ~0.38 mM.[28] This solution was stored in a glovebox freezer where it remained stable for several months. It should be noted that a freshly prepared catalyst produces the most consistent results in terms of NW quality. If stored for lengthy periods of time (several months), storage as a dilute solution results in particle aggregation, evident in absorption as a clear plasmon peak compared to that of the fresh catalyst which is small and barely observable (Figure S1 in the Supporting Information), as well as reduced SLS activity. For lengthy storage periods, concentrated solutions are preferred.

Synthesis of the Single-Source Precursor ([(PPh₃)₂Cu(µ-SePh)₂In(SePh)₂]). The [(PPh₃)₂Cu(µ-SePh)₂In(SePh)₂] precursor was synthesized according to a modified version of the procedure reported by Hepp et al.[30] Typically, the procedure was carried out as follows: C_6H_5SeNa was prepared by adding NaOEt (0.477 g, 7.00 mmol) in anhydrous MeOH (7.0 mL) to C_6H_5SeH (0.675 mL, 1.00 g, 6.37 mmol), which was already dissolved in 6.0 mL of anhydrous MeOH, followed by stirring of this clear yellow solution at room temperature for 20 h inside the drybox. A three-neck flask was then charged with the C_6H_5SeNa solution, and $InCl_3$ (0.352 g, 1.592 mmol) dissolved in 7.0 mL of anhydrous MeOH was rapidly

(26) Weare, W. W.; Reed, S. M.; Warner, M. G.; Hutchison, J. E. *J. Am. Chem. Soc.* **2000**, *122*, 12890–12891.

(27) Mitzi, D. B. *Inorg. Chem.* **1996**, *35*, 7614–7619.

(28) Grebinski, J. W.; Hull, K. L.; Zhang, J.; Kosel, T. H.; Kuno, M. *Chem. Mater.* **2004**, *16*, 5260–5272.

(29) Grebinski, J. W.; Richter, K. L.; Zhang, J.; Kosel, T. H.; Kuno, M. *J. Phys. Chem. B* **2004**, *108*, 9745–9751.

(30) Banger, K. K.; Jin, M. H. C.; Harris, J. D.; Fanwick, P. E.; Hepp, A. F. *Inorg. Chem.* **2003**, *42*, 7713–7715.

added, resulting in a clear solution (on some occasions a small amount of a white precipitate is also observed). The mixture was stirred inside the drybox and allowed to react for 12 h, yielding the $Na^+[In(C_6H_5Se)_4]^-$ precursor.

In a second reaction flask, Ph_3P (0.835 g, 3.184 mmol) dissolved in 4.0 mL of CH_2Cl_2 was added dropwise to a 10.0 mL CH_2Cl_2 solution or suspension of $[Cu(MeCN)_4]^+PF_6^-$ (0.593 g, 1.592 mmol) and allowed to stir at room temperature inside the drybox for 20 h. This cloudy solution was then filtered using a fine glass frit, yielding a clear solution containing the $[(Ph_3P)_2Cu(MeCN)_2]^+PF_6^-$ precursor.

The clear $[(Ph_3P)_2Cu(MeCN)_2]^+PF_6^-$ precursor solution was then gradually added to the $Na^+[In(C_6H_5Se)_4]^-$ precursor that was formed in situ, producing an immediate white precipitate. After 3 days of stirring at room temperature inside the drybox, all volatile materials were removed in vacuo. The $[(PPh_3)_2Cu(\mu\text{-SePh})_2In(SePh)_2]$ product was extracted with anhydrous 1,2-dichlorobezene (50 mL), and this yellow solution was filtered through a fine glass frit. Anhydrous pentane (~60 mL) was slowly added to the clear yellow product solution and left for 2 days, without further agitation inside the drybox, ultimately yielding pale yellow cube shaped crystals of the product (1.25 g, 59% yield based on $InCl_3$). The ^1H NMR spectrum of $[(PPh_3)_2Cu(\mu\text{-SePh})_2In(SePh)_2]$ agreed with previously published literature results:[30] ^1H NMR (300 MHz, $CDCl_3$, 25 °C, TMS) $\delta = 6.89$ (t, $J = 7.53$ Hz), 7.04 (t, $J = 7.26$ Hz), 7.19 (m), 7.28 (br d), 7.38 (m), 7.45 (m); ^{31}P NMR (121.4 MHz, $CDCl_3$, 25 °C, rel. to 85% aq H_3PO_4) $\delta = -0.45$ (s). EDX results are available in Figure S1 in the Supporting Information.

Synthesis of Cu−In−Se Nanowires from Multiple Source Precursors (MSPs) ("Reverse Injection"). $In(O_2CCH_3)_3$ (33.4 mg, 0.114 mmol), $Cu(O_2CCH_3)$ (14.0 mg, 0.114 mmol), TOP (2.0 mL), and oleic acid (0.106 mL, 94.43 mg, 1.145 mmol) were all added to a three-neck flask that was equipped with a reflux condenser inside the drybox. While stirring, this mixture was heated to 100 °C under vacuum on a Schlenk line and allowed to stir for an additional 15 min, at which time the bubbling solution turned from greenish-blue to faint yellow. After 15 min, this yellow solution was cooled to room temperature under nitrogen flow and then loaded into a syringe that contained TOPSe (0.229 mL, 0.229 mmol, 1.0 M solution). In a separate three-neck flask, 4.0 mL of TOP was degassed under vacuum for 5 min at room temperature, and after backfilling this flask with nitrogen, the solvent was heated to 300 °C while stirring. After stabilizing at 300 °C, the (Au)Bi catalyst (525 µL, 0.201 µmol, 0.38 mM) prepared above was rapidly injected into the hot TOP, with the solution turning faint brown and the temperature dropping to 281 °C. Immediately after injecting the catalyst solution, the yellow precursor solution was injected into the reaction flask, at which time the temperature dropped further to 250 °C and an immediate dark precipitate formed as the solution turned brownish-green in color. This reaction mixture was allowed to stir for an additional 4 min 30 s, whereby it took 4 min for the solution to reach 300 °C again. Immediately after, 30 mL of extremely cold toluene (liquid nitrogen cooled) was rapidly injected into the flask to quench the reaction after the heating mantle was removed. Rapid and complete injection of cooled toluene must take place in order to prevent aggressive solvent refluxing. The quenched reaction mixture was centrifuged (5 min at 4300 rpm), yielding a dark solid and a deep brownish-green supernatant. The weight of the washed and dried precipitate was 4.5 mg (12% yield), while that of the suspended material after precipitation with methanol followed by washing and drying was 3.3 mg (8.6% yield), resulting in a total yield of 7.8 mg (20.6% yield). TEM analysis confirmed that both fractions comprised NWs with little or no contribution from nanoparticles. In general, solids were purified for TEM analysis by suspending the solid in toluene (3 × 20 mL), with the aid of sonication, yielding a lighter colored supernatant after centrifuging in each case. After additional washing steps with acetone (3 × 20 mL) and hexanes (3 × 20 mL), the solid was finally resuspended in 7.0 mL of toluene and stored in the refrigerator.

Synthesis of Cu−In−Se Nanowires from $[(PPh_3)_2Cu(\mu\text{-SePh})_2In(SePh)_2]$. $[(PPh_3)_2Cu(\mu\text{-SePh})_2In(SePh)_2]$ (152 mg, 0.114 mmol) was dissolved in 1.0 mL of TOP with the aid of gentle heating on a hot plate stored inside the glovebox, generating a clear yellow solution. This yellow solution was allowed to cool to room temperature and then loaded into a syringe. In a separate three-neck flask, 5.0 mL of TOP and oleic acid (0.106 mL, 94.43 mg, 1.145 mmol), combined inside the drybox, were placed on the Schlenk line and degassed under vacuum for 15 min at room temperature, and after backfilling this flask with nitrogen, the solvent mixture was heated to 300 °C while stirring. After stabilizing at 300 °C, (Au)Bi catalyst (525 µL, 0.201 µmol, 0.38 mM) was rapidly injected into the hot TOP, with the solution turning faint brown and the temperature dropping to 286 °C. Immediately after injecting the catalyst solution, the yellow SSP solution was injected into the reaction flask, at which time the temperature dropped further to 280 °C and an immediate dark precipitate formed as the solution turned brownish-green in color. This reaction mixture was allowed to stir for an additional 4 min 30 s, whereby it took 3 min for the solution to reach 300 °C again. Immediately after, 30 mL of extremely cold toluene (liquid nitrogen cooled) was rapidly injected into the flask to quench the reaction after the heating mantle was removed. The quenched reaction mixture was centrifuged (5 min at 4300 rpm), yielding a dark solid and a deep brownish-green supernatant. The weight of the washed and dried precipitate was 12.1 mg (31% yield), while that of the suspended material after precipitation with methanol followed by washing and drying was 4.8 mg (13% yield), resulting in a total yield of 16.9 mg (44% yield). TEM analysis confirmed that both fractions comprised NWs with little or no contribution from nanoparticles. In general, solids were purified for TEM analysis by suspending the solid in toluene (3 × 20 mL), with the aid of sonication, yielding a lighter colored supernatant after centrifuging in each case. After additional washing steps with acetone (3 × 20 mL) and hexanes (3 × 20 mL), the solid was finally resuspended in 7.0 mL of toluene and stored in the refrigerator.

Materials Characterization. Purified nanowires were characterized by scanning electron microscopy (SEM), transmission electron microscopy (TEM), energy-dispersive X-ray spectroscopy (EDX), and X-ray diffraction (XRD). SEM images were obtained from nanowires mounted on a carbon coated Ni grid using a FEI Quanta 400 FEG-ESEM operating between 20 and 30 kV accelerating voltage, which was equipped with a Quanta-200/400 EDX system containing a Super UTW sapphire window detector operating with EDX Genesis Software version 4.61. The error associated with the SEM−EDX detector for each element is approximately 2−3 atom % for each element.

TEM images were obtained from nanowires mounted on a carbon coated 400 mesh Ni, Cu, or Mo grid imaged using a JEOL 2010 transmission electron microscope, equipped with a LaB_6 filament, operating at 200 kV accelerating voltage. EDX data were acquired using a Bruker XFlash SDD detector on the JEOL 2010 TEM. The error associated with the TEM−EDX detector for each element is approximately Cu (±2%), In (±3%), and Se (±2%). A Mo or Ni grid was used when EDX analysis was conducted for Cu. TEM analyses of the Au and (Au)Bi nanoparticles were also performed to confirm that the targeted diameters of ~1.5 and ~2.5 nm, respectfully, were obtained, and EDX of the (Au)Bi nanoparticles provided confirmation that Bi was successfully added to the Au seed particles (Figure S1 in the Supporting Information).

XRD data were acquired from NWs deposited on a background-less silicon wafer slide using a Rigaku Ultima III $\theta/2\theta$ powder diffractometer with Cu Kα radiation (1.5418 Å) and collected with a scintillation detector for 12 h over a 2θ range of 10−90° with an incremental angle of 0.02° at a scan rate of 0.10°/min. The experimental XRD patterns were refined by the Rietveld method using the General Structure Analysis System (GSAS) refinement

Scheme 1. Effect of (Au)Bi Nanoparticles and Ligand Choice on Reaction Product Obtained Using Multiple-Source Precursors
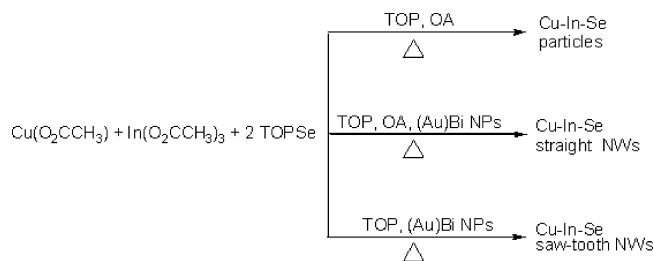
program.[31] The conventional Rietveld agreement indices, especially the weighted-refinement profile (wRp), were used as a statistical measure of the serial correlation in the powder pattern differences of the experimental data to the calculated fit as given by Hill et al.[32] and Durbin et al.[33]

Optical absorption measurements were conducted using a Cary 5000 UV—vis—NIR spectrophotometer (Varian). NWs were suspended in chloroform in $1 \times 1 \times 3$ cm quartz cuvettes. ^{1}H and ^{31}P NMR spectra were obtained on a Bruker Avance 300 MHz spectrometer operating at room temperature (300 MHz for ^{1}H and 121.4 MHz for ^{31}P).

Results and Discussion

Impact of the Metal Nanoparticle Catalyst on the Growth of Cu—In—Se NWs from Multiple-Source Precursors. When Cu, In, and Se precursors [In(acetate)$_3$, Cu(acetate), and TOPSe, respectively] were reacted at elevated temperature (270—300 °C) in the presence of coordinating ligands (oleic acid and trioctylphosphine, TOP), but in the absence of metal catalyst, aggregates of nanoscale isotropic particles were obtained (Scheme 1, top, and Figure 2a,b). In stark contrast, and partially confirming that the SLS growth mechanism is active in this system, addition of (Au)Bi (core)shell nanoparticles to the reaction mixture resulted in formation of Cu—In—Se NWs (Scheme 1, middle, and Figure 2c,d). The presence of catalyst tips on some of the NWs provided further confirmation that the growth mechanism is indeed SLS (Figure 2e). The absence of catalyst tips on other NWs is likely a result of NW/catalyst—tip separation that can occur during cooling of the reaction mixture, which is rapid and induced by addition of liquid-nitrogen-cooled toluene, or during NW workup. Occasionally, we obtain TEM images of NW catalyst tips that reveal a tenuous connection between the two components (Figure 2e, left) for which it seems likely that physical agitation of the NW sample (e.g., through sample sonication) might cause complete separation of the NW from its catalyst. In contrast, other images reveal an extensive, intact NW/catalyst—tip interface (Figure 2e, right).

The combination of low- and high-resolution TEM imaging also reveals additional aspects pertaining to the typical Cu—In—Se NW structure. The NWs are clearly single-crystalline, but with defects (Figure 2d—f). Further, the NWs are typically several micrometers in length, and an analysis of 45 NWs in TEM resulted in an average NW diameter of 24 ± 14 nm (Figure 2f). This diameter range is similar to that (5—40 nm) reported by Phok et al. for the physically templated approach[23] and is smaller than that obtained by either the molecular templated or

(31) Larson, A. C.; Von Dreele, R. B. *GSAS-General Structure Analysis Systems*; Los Alamos National Laboratory Report No. LAUR; Los Alamos National Laboratory: Los Alamos, NM, 2000; pp 86—748.
(32) Hill, R. J.; Flack, H. D. *J. Appl. Crystallogr.* **1987**, *20*, 356–361.
(33) Durbin, J.; Watson, G. S. *Biometrika* **1971**, *58*, 1–19.
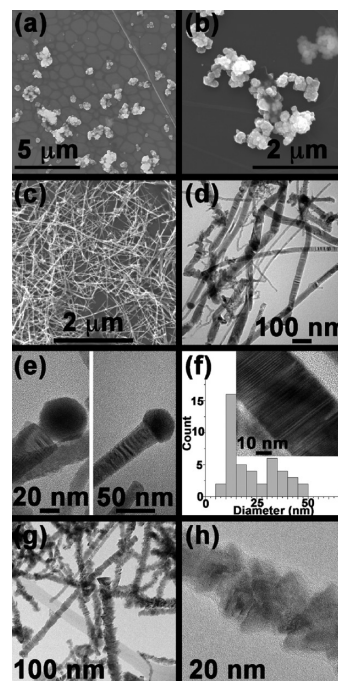
Figure 2. Reaction products resulting from experiments described in Scheme 1. (a,b) Cu—In—Se particles obtained in the absence of (Au)Bi nanoparticles. (c) SEM and TEM (d, e, and inset in f) images of straight Cu—In—Se nanowires obtained for a typical multiple-source precursor SLS reaction when both trioctylphosphine and oleic acid are present in the reaction. (f) Histogram depicting Cu—In—Se nanowire diameter distribution. (g,h) TEM images of sawtooth Cu—In—Se nanowires obtained for the multiple-source precursor SLS reaction when oleic acid is absent from the reaction mixture.

the VLS approaches reported by Yang et al. (50—100 nm)[22] and Peng et al. (20—200 nm),[20] respectively. Further, some of the SLS-grown NWs likely experience quantum-confinement effects as some of the observed diameters lie within the quantum-confined size regime, for which the onset is largely dictated by a Bohr exciton radius of 10.6 nm.[9] Nevertheless, we have clearly not achieved substantial control over NW diameter in this system. In general for SLS growth, the NW diameter is correlated with the diameter of the nanometal catalyst. In our case, the (Au)Bi core/shell nanoparticles that we employed were 2.7 ± 1.5 nm in size (Figure S1 in the Supporting Information). Although these possessed a similarly large distribution in size as compared to the related NWs ($\pm \sim 50\%$ for both catalyst and NW diameter distributions), the absolute values are plainly dissimilar (2.7 nm compared to 24 nm, respectively). However, where catalysts tips are evident on the Cu—In—Se NWs, the tip size and NW diameter are comparable in diameter, with the tip being slightly larger than the extending NW (Figure 2d,e), as is typical for both SLS and VLS-grown NWs. Thus, it is apparent that the catalyst particles grew during the course of the reaction. Further, it appears that the catalyst particles grew *prior to* NW nucleation and growth because little tapering is observed in the majority of the NWs. In other words, if the catalyst tip had continued to grow in size after NW growth had commenced, then the "youngest" sections of the NW (those closest to the tip) would be thicker than the "oldest" sections of the NW (those furthest from the tip), resulting in a tapered NW morphology. Such size-grading along the lengths of the NWs is mostly not observed here.

The apparently significant growth in catalyst size can be attributed to catalyst aggregation and/or catalyst swelling. The

Scheme 2. Effect of Reaction Temperature and Reactant Order-of-Addition on Reaction Product Obtained Using Multiple-Source Precursors
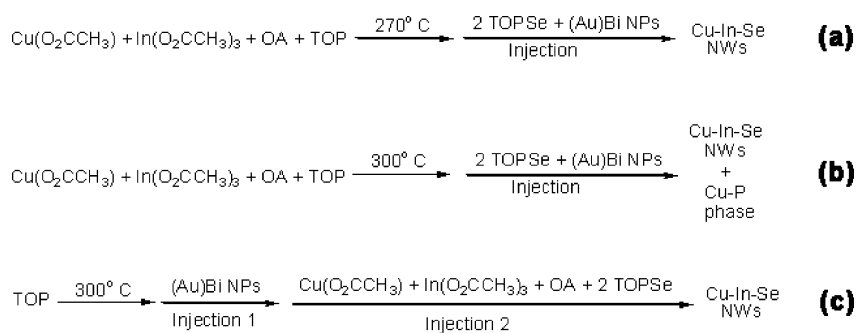
former process can result from the high reactivity and chemical instability of the very small metal nanoparticles at elevated temperatures, leading to particle agglomeration. The latter process can result from catalyst "swelling" that occurs prior to NW nucleation and growth during an initial alloying stage commonly observed for both SLS and VLS growth mechanisms.[7,21] During the alloying stage, precursor material (here, Cu−In−Se) dissolves into the metal catalyst until a point of supersaturation is reached at which time solid NW material nucleates and begins to grow. The extent of "extra" volume added to the originally small catalyst particle is, in this model, correlated with the solubility of the NW components in the molten metal. This issue is somewhat complicated in this case (and in much of the SLS literature), as the catalyst is a (core)shell particle with the core and shell materials possessing significantly different melting points. Irrespective of the exact mechanism of catalyst nanoparticle growth, its effect is clear: in this system, we have been limited to achieving NW diameters that, while smaller than several literature reports, are generally larger than that expected to exhibit quantum-confinement effects.

Impact of Ligand Identity on the Morphology of Cu−In−Se NWs Grown from Multiple-Source Precursors. From our initial results, it was apparent that the metal catalyst comprised a critical element supporting the desired NW growth. However, further investigations revealed that ligand effects also exerted a strong influence over nanocrystal morphology. In the case where we removed oleic acid but retained TOP as a coordinating ligand and reaction solvent ("excess TOP"), the resulting NWs were of very poor quality. Specifically, these NWs were not uniform in diameter along the length of the wire, exhibiting a sawtooth morphology (Scheme 1, bottom, and Figure 2g,h). This result was perhaps not surprising, as others have shown empirically that ligands can play key roles in the NW growth process and in determining NW morphology. For example, the presence of *n*-hexadecylamine in InP NW SLS reactions was credited with helping to improve InP NW crystallinity and reduce diameter distributions, while the addition of *n*-octylphosphonic acid was thought to prevent homogeneous nucleation of InP clusters.[7,21] In contrast, however, we did not see such improvements in NW quality with the addition of *n*-octadecylphosphonic acid (1:10 ODPA/TOP; 2:1 ODPA/total metals plus excess TOP) or trioctylamine (1:0 TOA/TOP, TOA only; 20:1 TOA/total metals), and in fact, these ligands appeared to result in significantly increased particle formation or in a combination of increased particle formation and sawtooth NW morphology, respectively. Interestingly, the addition of an amount of an alkylphosphine oxide (trioctylphosphine oxide, TOPO, 99%) approximately equivalent to the amount of TOP used in a typical reaction (1.5:1 TOPO/TOP; 30:1 TOPO/total metals plus excess TOP) resulted in *complete* suppression of

NW growth and exclusively particle formation similar to that observed for growth without a metal catalyst (Figure S2 in the Supporting Information). A lesser amount of TOPO (1:12 TOPO/TOP; 5:1 TOPO/total metals plus excess TOP) permitted NW growth (Figure S2 in the Supporting Information), but with significantly more particle formation compared to a TOP and oleic acid reaction (1:12 oleic acid/TOP; 5:1 oleic acid/total metals plus excess TOP; Figure 2c,d). On the basis of the reaction conditions explored, it was determined that the combination of TOP and oleic acid resulted in the least amount of particle formation and the straightest/smoothest NWs. This ligand combination was subsequently used in explorations of reaction temperature and reactant order-of-addition (below).

Impact of Reaction Temperature and Reactant Order-of-Addition on Phase-Formation in the Cu−In−Se System Using Multiple-Source Precursors. We explored two reaction temperatures (270 and 300 °C) in this work. Further, we investigated the impact of the reactant order-of-addition on NW properties. Specifically, we studied two distinct ways to bring reactants to temperature. In one method, we brought a mixture of the metal precursors, TOP, and oleic acid to the reaction temperature (270 or 300 °C) followed by rapid injection of the Se precursor and the catalyst nanoparticles combined in TOP (Scheme 2a,b). Alternatively, we heated TOP to 300 °C followed by rapid sequential injection of, first, catalyst nanoparticles in toluene then, second, a previously prepared mixture of metal−oleic acid precursors, selenium precursor and TOP (Scheme 2c). We refer to this latter approach as "reverse injection."

Both heating the metal precursors to 270 °C followed by injection of TOP-Se and (Au)Bu nanoparticles (Scheme 2a) and the reverse injection (Scheme 2c) approach resulted in a reasonably pure CuInSe$_2$ product (Figure 3a,b). Here, the powder XRD patterns indicate that the reaction products comprised a primary crystalline phase that is either chalcopyrite (tetragonal) or sphalerite (cubic) CuInSe$_2$ and a minor secondary phase that we attribute to Cu$_3$Se$_2$ (see detailed structure-refinement analysis below). Despite similarities in the XRD patterns, bulk EDX analyses of powder samples analyzed in the SEM revealed differences between the lower-temperature reaction product and the reverse-injection reaction product. The former product was rich in copper and poor in indium (33% Cu, 22% In, 45% Se), resulting in a total metals/selenium ratio of 1.22:1 rather than 1:1 expected for stoichiometric CuInSe$_2$, and an average composition of Cu$_{1.5}$In$_{1.0}$Se$_{2.0}$ (Figure S3 in the Supporting Information). The reverse-injection product was farther off-stoichiometry and substantially richer in copper and poorer in selenium (46% Cu, 18% In, 36% Se), resulting in a total metals/selenium ratio of 1.8:1 and an average composition of Cu$_{2.6}$In$_{1.0}$Se$_{2.0}$ (Figure S3 in the Supporting Information). The
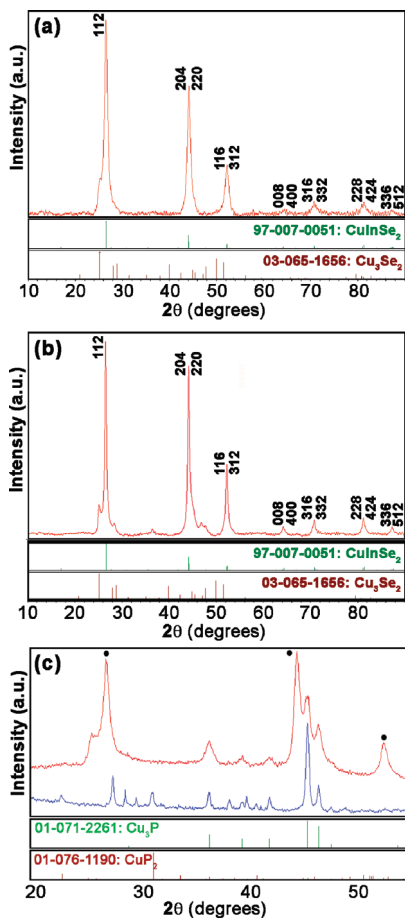
Figure 3. Powder XRD patterns of Cu−In−Se NW reaction products obtained using multiple-source precursors and different reaction temperatures and/or different reactant orders-of-addition. Vertical lines below indicate the reflections for the bulk material JCPDS patterns shown. (a) Reaction at 270 °C (Scheme 2a). (b) Reverse-injection reaction (Scheme 2c). (c) Top pattern, reaction at 300 °C (Scheme 2b), and bottom pattern, "control reaction" at 300 °C; Cu-oleate reacted with TOP, TOP-Se, and (Au)Bi catalyst in the absence of In. Dots in top pattern designate CuInSe$_2$ peaks.

observed Cu excess in both cases can, in part, be accounted for by the presence of the Cu$_3$Se$_2$ secondary phase that is evident in the respective XRD patterns (Figure 3a,b). This secondary phase contributes more significantly to the XRD pattern for the reverse-injection reaction product, agreeing with the observation from EDX analysis that this product is indeed relatively richer in Cu than the lower-temperature reaction product. Nevertheless, this phase appears to comprise a relatively minor fraction in either reaction product; therefore, it is also likely that the nominally "CuInSe$_2$" primary phase is itself not stoichiometric. Indeed, CuInSe$_2$ and related I−III−VI$_2$ compounds are well-known for their tendency to exhibit off-stoichiometry to an extent not seen for their II−VI binary counterparts.[10] Thus, the combined presence of a Cu-rich secondary phase (as evidenced in XRD powder patterns) and an off-stochimetric primary phase likely resulted in the observed average Cu−In−Se compositions for these reaction products. In addition to "bulk" SEM and XRD analyses, we explored this issue of NW stoichiometry further by obtaining compositional analyses of single NWs (see below).

In contrast with the lower-temperature and the reverse-injection reaction products, the reaction product obtained by heating the metal precursors to 300 °C followed by injection of TOP-Se and (Au)Bu nanoparticles (Scheme 2b) was less

clearly dominated by a primary "CuInSe$_2$" phase. The reaction product obtained using this method revealed an unexpected secondary phase in its XRD powder pattern, in addition to chalcopyrite or sphalerite CuInSe$_2$, the XRD pattern contained the Cu$_3$P phase (Figure 3c, top experimental pattern). The only source of phosphorus in this reaction was the ligand/solvent TOP. To confirm that TOP could act as a phosphorus source under these reaction conditions, we conducted a further reaction in which the Cu precursor was reacted with TOP, TOPSe, and the (Au)Bi catalyst at 300 °C in the absence of In. In this case, Cu$_3$P and, possibly, CuP$_2$ were formed almost exclusively (Figure 3c, bottom experimental pattern), confirming the competitive reactivity of TOP toward Cu in comparison with the Se reactant at the reaction temperature employed. Therefore, presumably as a result of the presence of the Cu−P phases in the reaction product, which lack Se and In, bulk EDX analysis in SEM revealed a composition of Cu$_{5.8}$In$_{1.0}$Se$_{2.0}$ and a metals/ Se ratio of 3.4:1.0 (Figure S3 in the Supporting Information). In addition to the extreme off-stoichiometry of the reaction product obtained for the higher-temperature reaction, this product was also characterized by substantially poorer shape control. While the reaction products obtained for the lower-temperature reaction and the reverse-injection reaction contained a small amount of particle contamination (as evidenced in both SEM and TEM images, for example, Figure 2c,d), large aggregates of particles comprised approximately 30−50% of the higher-temperature reaction product (Figure S3 in the Supporting Information).

Thus, a seemingly small change in the reaction temperature from 270 to 300 °C−or a change in the order of precursor addition−results in dramatic changes in composition and morphology. Using the "standard" reaction addition order (i.e., as opposed to the "reverse injection" approach), we obtained very different results when heating the Cu and In precursors (in the presence of oleic acid and TOP) to 270 °C compared to 300 °C. At the lower temperature, we were able to avoid formation of Cu$_3$P and to enhance the formation of NWs over aggregated nanoparticles, whereas, at 300 °C, phosphide phases dominated. In contrast, using the reverse-injection reactant order-of-addition, we were able to employ the higher reaction temperature and still avoid growth of Cu−P phases and significant particle formation. On the basis of these results, as well as our control reaction, it is clear that reaction conditions should be avoided that entail lengthy periods during which the Cu precursor is present with TOP above 270 °C in the absence of *either* Se or In precursors (such as during the heating of metal precursors to 300 °C in Scheme 2b or in our control reaction, respectively). Indeed, it was observed for the reaction shown in Scheme 2b that a visible color change occurred above 270 °C, resulting from significant precipitate formation, indicating particle formation prior to injection of the Se precursor and the (Au)Bi catalyst nanoparticles. Employing either the lower-temperature reaction (Scheme 2a) or the reverse-injection reaction (Scheme 2c) avoids this undesirable condition.

Single-NW Analyses of NWs Prepared from Multiple-Source Precursors Using the Reverse-Injection Scheme. Multiple EDX spot analyses were conducted along the length of 18 NWs, and single-spot analyses were performed on nine additional NWs. Representative along-NW analyses are shown in Figure 4. The majority of the NWs (22 of the 27 NWs analyzed; here, multiple-spot analysis results were averaged and compared to the single-spot data) exhibited compositions similar to those shown in Figure 4a,b, while a minority (4 of the 27
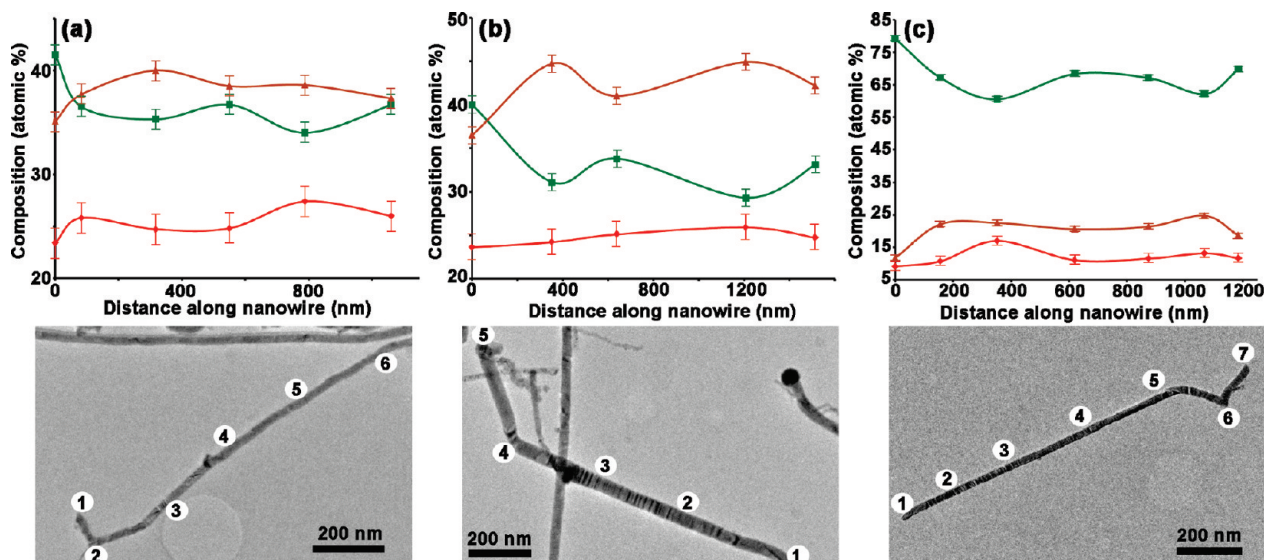
Figure 4. EDX multiple-spot analyses along the length of several representative NWs prepared from multiple-source precursors (brown, Se; green, Cu; red, In) are shown with their accompanying TEM images. (a,b) NWs representing the majority of the NWs analyzed: 22 out of 27. (c) NW representing a minority of the NWs analyzed: 4 out of 27. In all cases, lines are intended as guides to the eye and do not imply a statistical fit to the data. Error bars reflect the errors associated with the TEM−EDX detector for each element: Cu (±2%), In (±3%), and Se (±2%).

NWs analyzed) were extremely rich in Cu, similar to that shown in Figure 4c. One additional NW was devoid of any In and had an average composition of $CuSe_{1.2}$. The average composition obtained for the complete set of 27 NWs (Table S1 in the Supporting Information) was consistent with that determined by "bulk" SEM−EDX analysis—$Cu_{2.3}In_{1.0}Se_{2.0}$ compared to $Cu_{2.6}In_{1.0}Se_{2.0}$, respectively, confirming that the selection of NWs for single-NW analysis is representative of the ensemble sample. The good correlation between ensemble SEM−EDX analysis and single-NW TEM−EDX analysis also helps to confirm that the ensemble composition reflects the composition of the NW portion of the sample and not a minority particle fraction. Further, we observed that elemental atomic percentages varied considerably across the collection of 27 NWs (Cu (43 ± 12), In (20 ± 6.6), and Se (38 ± 7.3)). Interestingly, from NW-to-NW, the Cu and In deviated from their average values by 28 and 33%, respectively, while Se deviated by only 19% (Table S1 in the Supporting Information). Thus, Se incorporation was *on average* relatively more constant than metals incorporation.

Along any given NW, however, Se incorporation, together with metals incorporation, was observed to vary considerably (Figure 4), reflecting variable incorporation into NWs during the course of the reaction. Such changes in composition along the length of the NWs suggest that precursor incorporation into the (Au)Bi catalyst was not constant over the course of the reaction. It is unclear how general this observation of fluctuating composition along NW length is with respect to other SLS-grown NW systems, as very few examples of along-NW studies have been reported.[24,25] In one such example, fluctuations along the NW lengths were observed for nominally single-composition binary NW segments.[24] Interestingly, in almost all of the Cu−In−Se NWs that were analyzed along their lengths, Cu incorporation exhibited a clear "anti-trend" with respect to Se and, generally, In incorporation. Conversely, Se and In incorporation tended to trend together. In other words, when Cu levels increased from one point to the next in a given NW, Se levels, and generally In levels, decreased, and vice versa. An "anti-trend" in cation and anion incorporation is also evident in the EDX spot analysis data reported for ZnSe−ZnTe heterojunction

NWs.[24] We suggest that this observation along with the observation from both SEM and TEM−EDX analyses that the NWs were almost always Cu-rich imply that the manner in which Cu is incorporating—either at the stage of metal-flux incorporation or at the point of incorporation into the growing NW—is perhaps inhibiting Se and In incorporation. Alternatively, the Cu/Se anti-trend may represent a feature of $CuInSe_2$ itself, independent of the growth mechanism, as such a relationship was also evident in elemental analysis data for $CuInSe_2$ polycrystalline ingots grown by evaporation of the elements.[34]

In addition to analyzing the composition of the NWs, we determined the composition of several (Au)Bi catalyst tips. Specifically, EDX analysis of three catalyst tips still adhering to their NW ends revealed that these tips were Cu-rich (Figure S4 in the Supporting Information). The average atomic percentages and the standard deviations obtained for three tips were Cu (75 ± 5.0), In (7.0 ± 0.5), and Se (17 ± 5.0). (Bi was not taken into consideration when determining the composition of the catalyst tips, but it was present in the EDX spectra; see Figure S4 in the Supporting Information.) If these percentages are indeed representative of the composition of the flux medium during growth, it appears that excessive Cu incorporation into the NWs was favored by its dominating presence in the molten flux. In fact, it is perhaps interesting that the solid NW formed from such a flux was not even richer in Cu than the observed elemental ratio of $Cu_{2.3}In_{1.0}Se_{2.0}$. Presumably, the energy of formation of the NW product composition(s) provided a strong driver for compositions less rich in Cu than the "parent" flux. Examination of the available ternary phase diagrams suggests few stable Cu-rich phases, preferring, at lower temperatures, mixtures of $CuInSe_2$ and Cu−Se phases and, at higher temperature, mixtures of $CuInSe_2$ and Cu_3InSe_3 (Figure S5 in the Supporting Information). Our XRD data, compositional analyses, and experimental conditions are certainly consistent with the

(34) Merino, J. M.; Martin de Vidales, J. L.; Mahanty, S.; Diaz, R.; Rueda, F.; Leon, M. *J. Appl. Phys.* **1996**, *80*, 5610–5616.
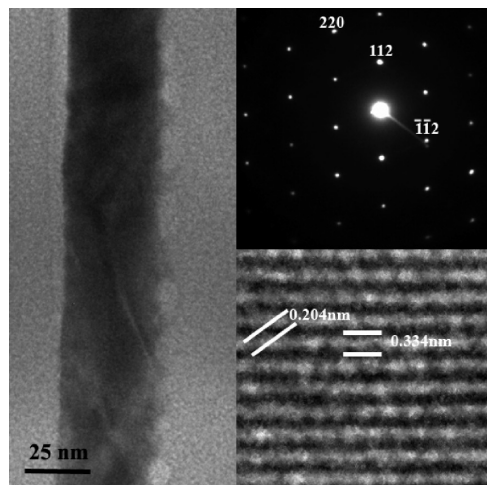
Figure 5. (left) TEM image of a multiple-source-precursor NW for which an SAED pattern (right, top) and a HRTEM image (right, bottom) were obtained and used to determine growth direction.

former, where in our case the Cu—Se phases comprise a smaller fraction of the sample compared to the CuInSe$_2$ phase.

The fact that the metal flux is so excessively rich in Cu is somewhat surprising. On the basis of simple thermodynamic considerations, as provided in the binary Bi—Cu, Bi—In, and Bi—Se phase diagrams, Cu is most distinctly not soluble (*at least as metallic Cu^0*) in Bi metal. On the contrary, at 300 °C, In^0 is miscible with Bi^0, while Se^0 is partially soluble, exhibiting also the tendency to form complex intermetallic compounds. Clearly, the binary phase diagrams do not accurately reflect the factors controlling incorporation of metal—organic precursors into SLS Bi catalysts. This added complexity contributes further to the complexity inherent to the development of appropriate reactant combinations and reaction conditions for the synthesis of ternary-phase SLS NWs.

Analysis of lattice-plane spacing in high-resolution TEM (HRTEM) images of the NWs revealed that the spacing parallel to the long axis of the NW is 0.334 nm, while that 35° to the long axis of the NW is 0.204 nm, consistent with the (112) and (220) planes of the CuInSe$_2$ chalcopyrite crystal structure (JCPDS No. 97-007-0051), respectively. Furthermore, all of the Cu—In—Se NWs examined (~10) grew along the [112] direction, which for a chalcopyrite structure means that the close-packed planes are perpendicular to the long axis. The crystalline structure and growth direction of the NWs were additionally confirmed by indexing of corresponding selected-area electron diffraction (SAED) patterns. These indexed along the [1−10] zone axis (Figure 5). In contrast with our observed growth direction, Peng et al.[13] reported that VLS-grown CuInSe$_2$ NWs grew along the [1−10] direction, which was confirmed by HRTEM images and the corresponding SAED pattern that was indexed along the [11−1] zone axis. This difference between the SLS and VLS-grown Cu—In—Se NWs likely results from the clear differences between these two synthetic approaches. For example, Cu—In—Se VLS NWs were grown at temperatures ~400 °C higher than those employed here, and the SLS NW growth was strongly influenced by the presence of interacting ligands in contrast with ligand-free VLS growth.

Primary and Secondary Crystalline Phases Analyzed Using Rietveld Refinement. To better assess the identity of the crystalline phases present in our reaction product patterns, we refined the experimental powder XRD patterns by the Rietveld

method using the General Structure Analysis System (GSAS) refinement program[31] (Figure S6 in the Supporting Information). Near-stoichiometric CuInSe$_2$ can exist in either of the two different crystal structures: tetragonal chalcopyrite or cubic sphalerite.[15,35] For each, the selenium anion sublattice is the same, but there are different possible cation orderings. In the case of sphalerite, the Cu and In atoms are randomly distributed in the cation sites, resulting in a cubic unit cell (space group $F\bar{4}3m$, high-temperature phase).[15,35] The chalcopyrite structure has a specific cation ordering and requires a tetragonal unit cell (space group $I\bar{4}2d$, low-temperature phase), with Cu occupying the (0,0,0) sites and In occupying the (1/2,1/2,0) sites of the cation sublattice.[15,35] We can index the major diffraction peaks of the experimental pattern to the (112), (204)/(220), (116)/(312), (008)/(400), (316)/(332), (228)/(424), and (336)/(512) reflections of the tetragonal chalcopyrite crystal structure (JCPDS No. 97-007-0051, CuInSe$_2$) (Figure 3). However, these major reflections are common to both the chalcopyrite and the sphalerite structures, with the additional reflections of (101), (103), (211), (105)/(213), and (301) that are specific to the chalcopyrite phase being absent. The absence of these reflections in our patterns does not itself preclude the possibility that the NWs are chalcopyrite. In a standard chalcopyrite pattern, the chalcopyrite-specific reflections are ~1/100th the intensity of the more intense lines. Furthermore, XRD lines broaden for nanocrystalline samples, making weak reflections more difficult to resolve. We also find that the lattice parameters calculated from the major phase of the refined XRD pattern are reasonably consistent with the lattice parameters of either the chalcopyrite or the sphalerite lattice parameters. Assuming a chalcopyrite structure, we calculated lattice parameters of $a = b = 5.79$ Å and $c = 11.55$ Å (compared to reported values of $a = b = 5.78$ Å and $c = 11.62$ Å: JCPDS No. 97-007-0051), or assuming a sphalerite structure, we calculated lattice parameters of $a = b = c = 5.78$ Å (compared to reported values of $a = b = c = 5.86$ Å: JCPDS No. 97-015-4411) (Table S2 in the Supporting Information). Despite this apparent ambiguity afforded by the XRD data, in the case of Cu—In—Se NWs prepared from multiple-source precursors, we are likely too far from stoichiometry to reasonably expect the chalcopyrite phase. Interestingly, this is not the case (near-stoichiometry is obtained) for the Cu—In—Se NWs prepared from the single-source precursor (below).

To more accurately assess the presence or absence of specific major and minor phases in the XRD patterns, we compared Rietveld agreement indices, especially the weighted-refinement profile (wRp—a statistical measure of the serial correlation between the experimental data and the calculated fit). A Rietveld refinement of the XRD pattern for NWs synthesized using multiple-source precursors and the reverse-injection approach and assuming either only the chalcopyrite or the sphalerite phases resulted in wRps of 7.5 and 8.5%, respectively. Both values are considered "good" indices of agreement, again verifying our inability to distinguish between these two phases with the available data. In contrast, however, Rietveld analysis was able to help us to distinguish between various options for the apparent secondary phases.

To help identify the secondary phase, additional refinements were conducted on the experimental XRD pattern, including in the refinement program CuSe$_2$ (JCPDS No. 01-082-0446), Cu$_3$P (JCPDS No. 01-071-2261), or Cu$_3$Se$_2$ (JCPDS No. 01-073-6051)

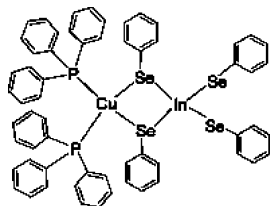(35) Stanbery, B. J. *Crit. Rev. Solid State Mater. Sci.* **2002**, *27*, 73–117.

Figure 6. Single-source precursor to Cu−In−Se NWs.

Figure 7. Single-source Cu−In−Se precursor SLS reaction product. (a,b) SEM and LRTEM images, respectively. (c) Histogram depicting Cu−In−Se NW diameter distribution. (d) TEM image of Cu−In−Se NW that has retained its (Au)Bi catalyst tip. (e) HRTEM image revealing crystalline nature of the NWs.

as the possible secondary phase (Tables S2 and S3 in the Supporting Information). Including either $CuSe_2$ or Cu_3P in the refinement procedure resulted in an increase in the wRp (7.5% → 11% or 7.5% → 14%, respectively (Tables S2 and S3 and Figure S7 in the Supporting Information), indicating a poorer fit, while including Cu_3Se_2 in the refinement procedure resulted in a decrease in the wRp (7.5% → 6.8%), indicating an improved fit. On the basis of these results and the observation that Cu_3Se_2 is the thermodynamically favored low-temperature Cu−Se phase (where $Cu_{2-x}Se$ and CuSe are known to react at room-temperature to produce it),[36,37] we concluded that Cu_3Se_2 is the likely dominant secondary phase. Additional Cu−Se phases were considered, but these produced even higher refinement values.

Synthesis of Cu−In−Se NWs Using a Single-Source Precursor (SSP): $[(PPh_3)_2Cu(\mu\text{-}SePh)_2In(SePh)_2]$. In general, establishing "ideal" reaction conditions for SLS NW growth in any newly explored system is complicated by several factors, which are likely exacerbated in the more complex ternary system studied here. It has been suggested in a few reports that these factors include (1) differences in precursor reactivities and their characteristic, as well as catalyst-assisted,[7] decomposition pathways that can lead to the production of poorly understood precursor intermediates,[7,21,38] (2) differences in precursor solubility in the molten Bi catalyst that could result in composition fluctuations within the catalyst prior to supersaturation and NW growth, as well as affect the length of the "incubation" time prior to onset of NW growth,[7,38,39] and (3) the continuous change in precursor concentrations over time as precursor is consumed in the reaction.[21,38,39]

In an attempt to address some of these complicating factors, especially the former two, we have explored—in addition to multiple-source precursors as described above—a single-source precursor for the SLS synthesis of $CuInSe_2$ NWs. Single-source precursors are unique compared to their multiple-source counterparts in that the desired bonds of the product material are "pre-established." Here, we employed $[(PPh_3)_2Cu(\mu\text{-}SePh)_2In\text{-}(SePh)_2]$,[14,30] where the precursor "core" comprises Cu and In bound through two bridging Se atoms (Figure 6). In the case of single-source precursors, it is possible that reactive intermediates retain their core structure, thereby simplifying and "equalizing" precursor reactivities, as well as incorporation of the desired elements into the SLS molten metal flux.

Similar to the reverse-injection approach used for the multiple-source precursor system (Scheme 2c), the single-source precursor was injected into a mixture of hot TOP and oleic acid (270 or 300 °C) immediately following injection of the (Au)Bi
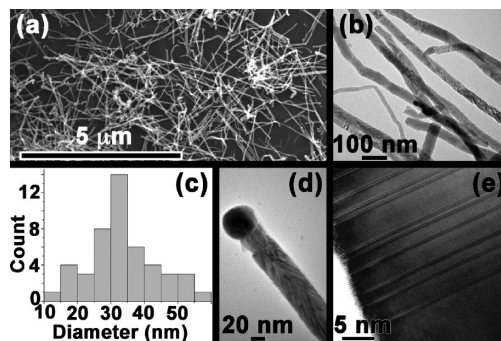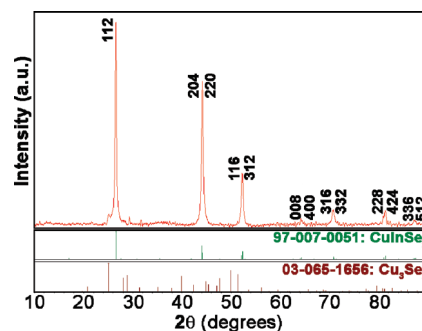

Figure 8. Powder XRD pattern of Cu−In−Se NW reaction product obtained using the single-source precursor. Vertical lines below indicate the reflections for the bulk-material JCPDS patterns shown.

catalyst particles. Following workup, the product comprised NWs that were 33 ± 10 nm in diameter and up to several micrometers in length, with little contamination from nanoparticles or particle aggregates (Figure 7a−c). The NW yield (44%) was approximately double that afforded by the multiple-source-precursor approach (20.6%) (Experimental Section). Where catalyst particles were present at the NW tips, the NW diameters were proportional to the final catalyst size (Figure 7d). The larger average diameter obtained for the SSP reaction product compared to those obtained using the MSP approach may imply a longer induction period prior to nucleation and growth of a NW. No wires were grown in the absence of catalyst using the SSP, again, along with the direct observation of catalyst tips, confirming that the mechanism of growth was indeed SLS growth. Significantly, EDX analysis in SEM of the isolated powder revealed that the SSP reaction product was nearly stoichimetric, in contrast with its MSP counterparts. Specifically, average atomic percentages of 27% (Cu), 26% (In), and 47% (Se) were obtained that correspond to a calculated composition of $Cu_{1.1}In_{1.1}Se_{2.0}$ (Figure S8 in the Supporting Information) and a metals/Se ratio of 1.1:1.0.

Powder XRD analysis of the SSP reaction product demonstrated that the SSP approach produces a cleaner product compared to any of the MSP variations, with secondary phases comprising a very minor component (Figure 8). As in the case of the MSP reaction products, it cannot be definitively determined that the primary phase is the chalcopyrite $CuInSe_2$ phase. Again, only the "major reflections" are observed, and those reflections that are specific to the tetragonal phase are absent. Indeed, the primary phase indexed well to both the tetragonal chalcopyrite (JCPDS No. 97-007-0051, $CuInSe_2$; Figure 8) and

(36) Zhang, S.-Y.; Fang, C.-X.; Tian, Y.-P.; Zhu, K.-R.; Jin, B.-K.; Shen, Y.-H.; Yang, J.-X. *Cryst. Growth Des.* **2006**, *6*, 2809−2813.
(37) Shohno, M.; Ohtani, T. *J. Solid State Chem.* **2004**, *177*, 3886−3890.
(38) Fanfair, D. D.; Korgel, B. A. *Cryst. Growth Des.* **2008**, *8*, 3246−3252.
(39) Kolasinski, K. W. *Curr. Opin. Solid State Mater. Sci.* **2006**, *10*, 182−191.
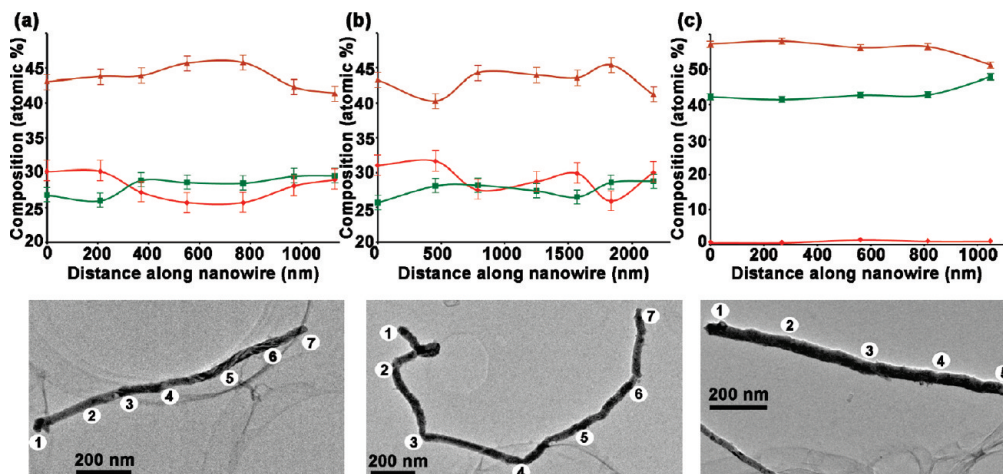
Figure 9. EDX multiple-spot analyses along the length of several NWs prepared using the single-source precursor (brown, Se; green, Cu; red, In) are shown with their accompanying TEM images. (a,b) NWs representing the majority of the NWs analyzed, i.e., 8 out of 12; TEM–EDX compositional analyses are in agreement with ensemble SEM–EDX results. (c) NW representing a minority of the NWs analyzed, 4 out of 12; TEM–EDX compositional analyses are not in agreement with ensemble SEM–EDX results, implying that such NWs indeed represent a minority of the sample. In all cases, lines are intended as guides to the eye and do not imply a statistical fit to the data. Error bars reflect the errors associated with the TEM–EDX detector for each element: Cu ($\pm 2\%$), In ($\pm 3\%$), and Se ($\pm 2\%$). [Note: In levels in (c) are too low to be considered reliable.]

the cubic sphalerite (JCPDS No. 97-015-4411) crystal structures, where Rietveld refinement provided similar wRp's for the tetragonal and cubic variations: 9.95% and 11.40%, respectively (Figure S9 and Table S4 in the Supporting Information). The lattice parameters calculated from the primary phase of the refined XRD pattern are $a = b = 5.78$ Å and $c = 11.60$ Å, assuming a tetragonal crystal structure, and $a = b = c = 5.78$, assuming a cubic crystal structure. Additional refinements were conducted that included possible secondary phases into the process. When $CuInSe_2$ and $CuSe_2$ were considered together in the refinement process, the wRp value jumped from 9.95 to 21.33%, with other refinement parameters worsening, as well, such as reduced χ^2, which changed from a reasonable 14.14 to an unacceptable 64.78. On the contrary, when $CuInSe_2$ and Cu_3Se_2 were considered together, both the wRp and the reduced χ^2 values decreased, indicative of an improved fit (7.68% and 8.35, respectively, Table S4 in the Supporting Information). Thus, Cu_3Se_2 appears to be the likely secondary phase, rather than $CuSe_2$. This is in agreement with the observations made for the MSP systems and, likely, for similar reasons as described previously.

Single-NW EDX Analyses of NWs Prepared Using the Single-Source Precursor. EDX was conducted at multiple locations along the length of 12 NWs. Representative along-NW analyses are shown in Figure 9. Eight of these NWs exhibited a Cu/In/Se ratio consistent with a slightly metals-rich "CuInSe$_2$" reaction product (Figure 9a,b). Specifically, the average composition for these NWs was $Cu_{1.3}In_{1.3}Se_2$ (Table S5 in the Supporting Information), revealing equal incorporation of the metals, respectively, in contrast with the MSP NWs for which Cu clearly dominated the reaction product. Similar to the MSP result, the metals/Se ratio for the SSP NWs revealed an overall metals rich composition, but to a considerably lesser extent—1.7:1.0 for MSP NWs ($Cu_{2.3}In_{1.0}Se_{2.0}$) compared with 1.3:1.0 for SSP NWs (or only 1.1:1.0 considering the SEM–EDX results discussed above; $Cu_{1.1}In_{1.1}Se_{2.0}$). Although along-NW variability was similar to that observed for the MSP NWs, *between-NW variability* was considerably reduced, with In and Se varying from NW-to-NW by only <5% and Cu by 10% (Table S5 in the Supporting Information). Thus, the SSP
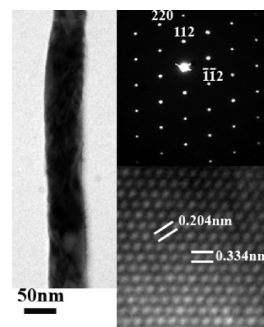

Figure 10. TEM image (left) of a single-source-precursor NW for which an SAED pattern (right, top) and a HRTEM image (right, bottom) were obtained and used to determine growth direction.

approach appears to have allowed for more consistent incorporation of the three elements. Nevertheless, occasionally, examples of "catastrophic" failure-to-incorporate were observed in the single-NW EDX analyses. Specifically, 4 of the 12 NWs analyzed surprisingly showed *no In content*. These NWs were, within the error of the analysis, entirely Cu–Se—ranging from copper-rich to selenium-rich. An example of this type of NW is shown in Figure 9c. Given the consistency of the SSP NWs that contained In, the apparent absence of "intermediate" compositions (i.e., only Cu/In ratios of 1:1 or 1:0 were observed), the near-stoichiometric composition obtained by "bulk" SEM–EDX analysis, and the relatively clean XRD pattern, these four Cu–Se NWs were considered not to be representative of the sample and were, therefore, not included when determining the between-NW variability described above.

HRTEM images of these NWs also show distinct lattice fringes (Figure 10). The spacing of the lattice planes parallel and 35° to the long axis of the NW is 0.334 and 0.204 nm, consistent also with the (112) and (220) planes, respectively, of the stochiometric chalcopyrite structure. Similarly, all of the NWs examined grow along the [112] direction. The crystalline structure and growth direction of these NWs were confirmed by the corresponding SAED pattern, which was also indexed along the [1−10] zone axis (Figure 10).
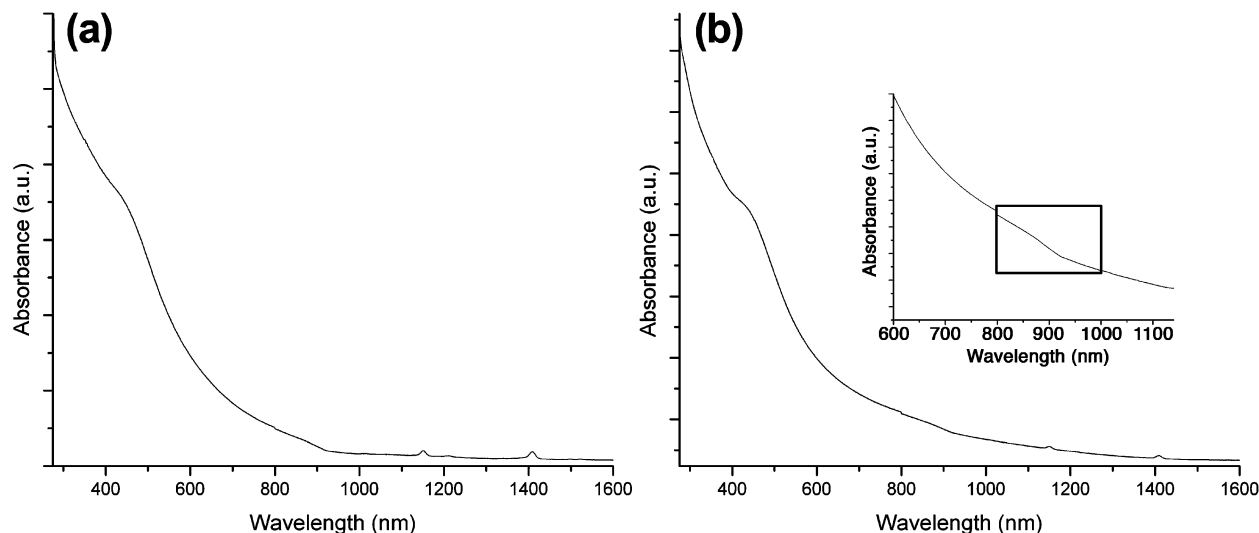
Figure 11. Absorption spectra of (a) multiple-source-precursor and (b) single-source-precursor Cu−In−Se NWs.

Cu−In−Se NW Optical Properties. The absorption spectra of MSP and SSP Cu−In−Se NWs in chloroform are presented in Figure 11. Absorption onsets in the near-infrared for both systems are qualitatively consistent with the CuInSe$_2$ bulk band gap of 1200 nm (1.03 eV). However, some discrepancies are evident. For the SSP NWs, absorption begins at roughly 1400 nm, which is red of (lower energy than) the bulk CuInSe$_2$ band gap. The presence of a long, weak absorption tail at energies lower than the band gap energy may be indicative of the existence of defect states within the band gap.[40,41] It is perhaps surprising that of the two systems—MSP and SSP—the SSP system possesses this red-tail absorption because the SSP NWs were near-stoichiometric. In contrast, *nonstoichiometry* has previously been associated with such absorption profiles, though the specific nature of the nonstoichiometry (i.e., Cu-rich versus In-rich) appears to play a significant part in determining the precise effects on absorption.[41]

The absorption spectrum for the MSP NWs is itself somewhat anomalous. Here, although absorption does appear to onset at ∼1200 nm, it remains relatively flat in this region and only abruptly transitions at ∼920 nm. Given the relatively large diameters observed for both NW systems, and especially for the SSP system, quantum-confined blue-shifting is not expected in either case. Indeed, previously reported CuInSe$_2$ nanoparticles comparable in diameter to our NWs (16 nm) showed no evidence of quantum-confinement effects,[42] while much smaller nanoparticles (4.5 nm diameter) showed clear blue-shifting.[43] Whatever the origin of this feature, it is also evident, though less clearly, in the SSP spectrum as a small transition in slope starting at ∼920 nm (Figure 11b, inset). Despite these various peculiarities, the spectra are consistent with CuInSe$_2$ absorption and reveal the potential for these materials as solar energy harvesters, where ∼1030 nm (1.2 eV) is considered to be the optimal band gap for single-junction solar cells.[42]

Conclusions

In this study, we have demonstrated for the first time the synthesis of ternary Cu−In−Se NWs using the solution-phase SLS growth method and have compared the efficacy of multiple- and single-source precursors.[44] The compositions of the NWs prepared in this way ranged from significantly Cu-rich to nearly stoichiometric CuInSe$_2$, depending upon precursor identity, as well as choice of coordinating ligands, temperature and reactant order-of-addition. All NWs were found to be crystalline and to grow along the [112] growth direction. Significant differences were observed, however, in terms of average NW composition, between-NW compositional variability, and "contamination" by secondary phases (especially Cu$_3$Se$_2$). In contrast with the NWs prepared using multiple-source precursors, those synthesized using the single-source precursor provided nearly stoichiometric CuInSe$_2$ with little compositional NW-to-NW variability and an almost phase-pure powder XRD pattern. Experiments to determine the photoresponse from these new, chemically synthesized NWs are underway toward an assessment of their utility as building-block nanomaterials for applications in energy harvesting.

Supporting Information Available: SEM, TEM, XRD, EDX, and NMR. This material is available free of charge via the Internet at http://pubs.acs.org.

JA905730N

(40) Cohen, E.; Sturge, M. D. *Phys. Rev. B* **1982**, *25*, 3828.
(41) Shioda, T.; Chichibu, S.; Irie, T.; Nakanishi, H.; Kariya, T. *J. Appl. Phys.* **1996**, *80*, 1106–1111.
(42) Tang, J.; Hinds, S.; Kelley, S. O.; Sargent, E. H. *Chem. Mater.* **2008**, *20*, 6906–6910.
(43) Malik, M. A.; O'Brien, P.; Revaprasadu, N. *Adv. Mater.* **1999**, *11*, 1441–1444.
(44) Sun, J.; Buhro, W. E. *Angew. Chem. Int. Ed.* **2008**, *47*, 3215–3218.